Optical diffraction tomography microscopy with transport of intensity equation using a light-emitting diode array

CrossMark

Jiaji Li[a,b], Qian Chen[b], Jialin Zhang[a,b], Zhao Zhang[a,b], Yan Zhang[a,b], Chao Zuo[a,b,*]

[a] Smart Computational Imaging (SCI) Laboratory, Nanjing University of Science and Technology, Nanjing, Jiangsu 210094, China
[b] Jiangsu Key Laboratory of Spectral Imaging & Intelligent Sense, Nanjing University of Science and Technology, Nanjing, Jiangsu 210094, China

ARTICLE INFO

ABSTRACT

Optical diffraction tomography (ODT) is an effective label-free technique for quantitatively refractive index imaging, which enables long-term monitoring of the internal three-dimensional (3D) structures and molecular composition of biological cells with minimal perturbation. However, existing optical tomographic methods generally rely on interferometric configuration for phase measurement and sophisticated mechanical systems for sample rotation or beam scanning. Thereby, the measurement is suspect to phase error coming from the coherent speckle, environmental vibrations, and mechanical error during data acquisition process. To overcome these limitations, we present a new ODT technique based on non-interferometric phase retrieval and programmable illumination emitting from a light-emitting diode (LED) array. The experimental system is built based on a traditional bright field microscope, with the light source replaced by a programmable LED array, which provides angle-variable quasi-monochromatic illumination with an angular coverage of $\pm$ 37 degrees in both *x* and *y* directions (corresponding to an illumination numerical aperture of ~0.6). Transport of intensity equation (TIE) is utilized to recover the phase at different illumination angles, and the refractive index distribution is reconstructed based on the ODT framework under first Rytov approximation. The missing-cone problem in ODT is addressed by using the iterative non-negative constraint algorithm, and the misalignment of the LED array is further numerically corrected to improve the accuracy of refractive index quantification. Experiments on polystyrene beads and thick biological specimens show that the proposed approach allows accurate refractive index reconstruction while greatly reduced the system complexity and environmental sensitivity compared to conventional interferometric ODT approaches.

1. Introduction

In microscopy imaging, the phase carries important information about the object's structure and optical properties, while this information cannot be directly visible. The typical examples of visualization methods are phase contrast microscopy [1] and differential interference contrast microscopy [2], which has has been widely used in biomedical studies. But these techniques do not provide quantitative maps of phase change, making quantitative analysis and the interpretation difficult.

Interferometric method, such as digital holography microscope (DHM) [3,4], makes it possible to quantitatively measure the phase delay introduced by the heterogeneous refractive index distribution within the specimen. Nevertheless, conventional interferometry typically relies on highly coherent laser source, and the speckle noise also prevents the formation of high quality images. Over the past decades, more advanced quantitative phase microscopy techniques, that allow for self-interference under white-light illumination, have been reported

to greatly improve the spatial resolution and imaging quality of the phase measurement [5–8]. On a different note, non-interferometric quantitative phase imaging can be realized with the transport of intensity equation (TIE) [9–15] only using object field intensities at multiple axially displaced planes. Furthermore, the phase can be uniquely determined by solving the TIE without complicated interferometric optical system and phase unwrapping.

Although the quantitative phase can provide reliable information about biological samples with the methods mentioned above, the measured phase only represents the optical path length along the axial direction, making the detailed volumetric information inside the sample inaccessible. Three dimensional (3D) imaging could be implemented by recording the images of specimen at various illumination angles. The 3D refractive index map of the specimen could then be reconstructed using the set of angular images. There are two ways to achieve the relative change of illumination angle. First, a sample of interest can be rotated, and the images of diffracted light field at

different rotation angles can be used to reconstruct the 3D refractive index map of the sample [16–19]. Sample rotation enables the entire angular coverage, but the mechanical rotation inevitably makes the sample unstable, called radial run-out [17]. This method is more suitable for certain solid non-biological objects such as optical fibers. A special sample cuvette is required for the imaging of living biological cells in rotating method [20,21]. The second method is illumination scanning, the mirror mounted on a galvanometer or a piezoelectric transducer is typically used as a beam rotator, controlling the angle of the illumination beam that impinges onto a sample [22–26]. In recent years, the liquid crystals spatial light modulator (SLM) [27] and digital micro-mirror device (DMD) [28,29] have been utilized as a beam rotator for faster imaging speed and more stable beam controlling. Besides, tomographic imaging has also been implemented based on the lens-free platforms, providing both depth-resolved imaging capability as well as a very large field of view [30,31]. Nevertheless, these lens-free tomographic methods still depend on mechanical movement and laser illumination, and the resolution of 3D imaging also needs to be improved compared to existing high-NA conventional microscopy. Due to the finite numerical aperture of an objective, the lack of complete angular coverage leads to poorer axial resolution than the transverse resolution of the beam rotation method. For a specimen with prior knowledge, various algorithms have been developed to solve the problem of missing angle information [32,33].

The choice of 3D reconstruction algorithm is crucial to the spatial resolution and quantification of final reconstructed refractive index map. If the phase of transmitted field is interpreted as a line integral of the refractive index along the propagation direction for X-ray computed tomography (CT), then the filtered back-projection algorithm based on the inverse Radon transform can be applied [34]. Within the framework of diffraction tomography theory, the effect of diffraction is explicitly taken into account. Optical diffraction tomography (ODT) was first theoretically proposed by E. Wolf [35] in 1969 and the geometrical interpretation of ODT was presented by Dändliker and Weiss [36]. Lately, there have been some significant technical advances in diffraction tomography imaging for label-free 3D cell imaging [22–24,37,38]. Approximations such as the Born or Rytov approximation have been employed in ODT imaging to make the relationship between the 3D scattering potential and the two dimensional (2D) measured field straightforward [24,34,39].

However, most existing optical tomographic methods generally rely on interferometric implementation for phase measurement and sophisticated mechanical systems for sample rotation or beam scanning. Thus, the accuracy of phase measurement may be disturbed by the coherent speckle, environmental vibrations, and mechanical error during data acquisition process. To overcome these limitations, we use a light-emitting diode (LED) array as the illumination source within a

conventional transmission microscope in this work. A single LED of the programmable source is turned on sequentially to generate the variable angle beam covering the angular range from −37 to 37 degrees. It should be noted that a similar experimental configuration, based on the illumination of a LED array, has been widely implemented in Fourier ptychographic microscopy for high-resolution and wide-field imaging [40–43]. Using two intensity images taken at distinct planes along the optical axis for each incident angle, the angular complex field images can be directly retrieved via the TIE. Moreover, the positional misalignment correction of the LED array is presented to correct some misplaced frequency spectrum components in 3D Fourier spectrum. The Rytov approximation, which is less restrictive than the Born approximation, will be chosen to simplify the relationship between the 3D scattering potential and the 2D measured field for biological cells imaging in this paper.

The proposed approach gets rid of coherent laser illuminations and complicated mechanical system for sample rotation and beam scanning, and bypasses the difficulties in phase unwrapping, as is common for interferometric methods. These advantages make it a competitive and powerful alternative to interference techniques for various microscopy applications in micro-optics inspection, life sciences, and biophotonics. Precise refractive index measurement of a micro polystyrene bead validates the principle and demonstrates the accuracy of this method. The experimental results on investigation of unstained Pandorina morum and human cancer cells are then presented, suggesting that the method developed can provide promising applications in the disease diagnosis and morphology study of cellular processes.

2. Experimental setup

Fig. 1 shows the schematic diagram of system illumination, the positional misalignment of LED array, and the photograph of imaging system. The illumination component of conventional microscope is replaced by a 15×15 programmable LED array beneath the specimen. It should be noted that the original LED array contains totally 64×64 LED elements, and only a fraction of them (the 15×15 LEDs on the upper right corner) are used for sample illumination, as shown in Fig. 1(c). Each LED can provide approximately spatially coherent quasi-monochromatic illuminations with narrow bandwidth (central wavelength $\lambda = 530$ _nm_, ~ 20 _nm_ bandwidth). The light emitted from each LED can be approximately treated as a plane wave for each small image region of the specimen. The distance between every adjacent LED elements is 2.5 _mm_, and the LED array is placed 23 _mm_ away from the sample stage. Thus, the maximum illumination angle of LED array is about 37 degrees in both x or y directions.

In our system, the LEDs in array are turned on sequentially and controlled by a custom-built Field Programmable Gate Array (FPGA)
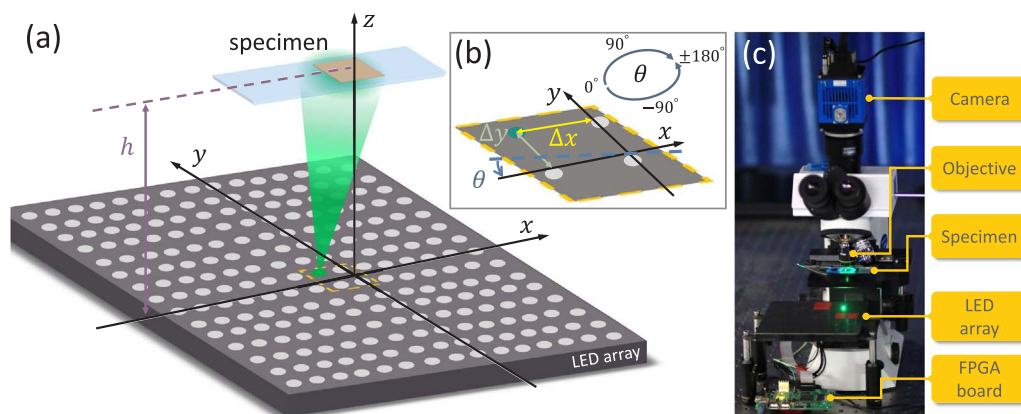

Fig. 1. (a) Schematics explaining of system illumination. A LED array is placed under the specimen and the distance from specimen to LED array is 23 mm. Spacing between adjacent LED elements is 2.5 mm. (b) The system error of translation Δx, Δy and rotation angle θ caused by the misplaced LED array. (c) Photograph of the imaging system. The crucial parts of setup in this photo are marked with the yellow boxes.

board. The total time of single tomographic image acquisition is about 37 s (~ 250 ms for each luminous LED). The microscope is equipped with a scientific CMOS (sCMOS) camera (PCO.edge 5.5, 2560×2160 pixels, 6.5 μm pixel pitch) and an universal plan super-apochromat objective (Olympus, UPlan SAPO $20 \times$, NA $= 0.75$). The LED array is synchronized with camera under each different illumination angle. Fig. 1(b) illustrates the enlarged map of the misplaced LED array which will cause the translation error Δx, Δy and rotation error θ relative to the optical axis. The detail theory of misalignment correction for LEDs is presented in subSection 3.3. The photograph of imaging system is shown in Fig. 3(c) and the crucial parts of setup in this photo are marked with the yellow boxes.

3. Principle

3.1. TIE for phase retrieval

In order to obtain the quantitative phase of object, some interferometric and non-interferometric approaches can be used for phase measurement. In previous work, the heterodyne Mach-Zehnder interferometer is employed commonly for recording amplitude images as well as phase images [22–24]. But these interferometric phase reconstruction methods still depend on vibration-sensitive interferometric device, and the speckle noise of laser light source precludes the spatial resolution of measurements. On the other hand, non-interferometric deterministic approaches could be realized by solving TIE [9]. In the paraxial regime, wave propagation is mathematically described by the Fresnel diffraction integral [44], while the relationship between the intensity and phase during wave propagation can be described by TIE:

$$-k\frac{\partial I(\boldsymbol{r})}{\partial z} = \nabla_{\perp}\cdot[I(\boldsymbol{r})\nabla_{\perp}\phi(\boldsymbol{r})] \tag{1}$$

where k is the wave number $2\pi/\lambda$, $I(\boldsymbol{r})$ is the intensity image at in-focus plane, $\nabla_{\perp}$ denotes the gradient operator over the transverse direction $\boldsymbol{r}$, and $\phi(\boldsymbol{r})$ represents the phase of object. The left hand of TIE is the spatial derivative of intensity at the in-focus plane along z axis. The longitudinal intensity derivative $\partial I/\partial z$ can be estimated through difference formula $(I_1 - I_2)/\Delta z$, where I_1 and I_2 are the two captured intensity images and Δz is the distance between two axially displaced planes. The part of right hand is a second order elliptic partial differential equation, and phase distribution at the image plane can be retrieved by solving the TIE using fast discrete cosine transform (DCT) under homogeneous Neumann boundary conditions [45]. By introducing the Teague's auxiliary function $\nabla_{\perp}\psi(\boldsymbol{r}) = I(\boldsymbol{r})\nabla_{\perp}\phi(\boldsymbol{r})$, the TIE is convert into the following two Poisson equations:

$$-k\frac{\partial I(\boldsymbol{r})}{\partial z} = \nabla_{\perp}^2\psi \tag{2}$$

and

$$\nabla_{\perp}\cdot(I^{-1}\nabla_{\perp}\psi) = \nabla_{\perp}^2\phi \tag{3}$$

The solution for ψ could be obtained by solving the first Poisson equation [Eq. (2)], thus the phase gradient can be obtained as well. The second Poisson equation [Eq. (3)] is used for phase integration. By solving the two Poisson equations with use of fast DCT [46], the phase $\phi(\boldsymbol{r})$ can be uniquely determined apart from an arbitrary additive constant, which is trivial for quantitative phase imaging. Generally, under simplified homogeneous Neumann boundary conditions (assuming zero phase change at the image boundary), the TIE is solved for the quantitative phase. The choices of this boundary conditions are reasonable since the samples in the region of interest (ROI) image are isolately distributed, thus the disturbance from samples located at the edge of image can be safely neglected.

3.2. Diffraction tomography with LED array

In transmission imaging, the absorption coefficient and refractive index of objects affect both amplitude and phase of the field, so both amplitude and phase images of the transmitted field must be retrieved. But the wave equation is still too complicated to extract the structure of objects from the transmitted E-field images [24]. Thus, there are some approximations, like Born and Rytov approximations, can be employed to simplify the relationship between the 3D scattering potential and the 2D measured complex field.

These two kinds of approximations are valid for different situations. It has been demonstrated that the Born approximation to be valid while the total phase delay of the measured field induced by the specimen is less than $\pi/2$ [24,34], which in turn requires the size of the object to be small and the refractive index contrast to be low. On the contrary, the Rytov approximation is independent of the sample size and total phase shift, but the gradient of phase. That is, the Rytov approximation is valid in diffraction tomographic imaging as long as the phase gradient of sample is small enough. Due to the diffraction tomography comparison results based on the Born and Rytov approximations have been presented in previous work [39,24], we will not compare performance of these two approximations in this paper. And we implement the diffraction tomography algorithm based on the Rytov approximation in our imaging system since the phase delay induced by typical biological cell in the medium can easily exceed $\pi/2$ [37].

For the acquisition of angular complex E-field images, the illumination scanning of LED array is used for diffraction tomography imaging. As the illumination source, each LED element of the programmable array generates an incident wave. In order to achieve isotropic transverse resolution and higher illumination utilization of LED array, only LEDs falling within a circular region of the array are used, as illustrated in Fig. 2(a). Another reason for using circular illumination is that the pupil of objective is also circular in shape. There are 149 LEDs in the dashed circle and the beam of LED outside the circle is ignored. Fig. 2(b) shows the 2D diagram of the diffraction tomography imaging setup based on a conventional microscopy using the LED array. The light from the jth LED scatters through the sample and exits its top surface. Then the field is propagated and limited by the finite microscope aperture at the microscope back focal plane. Finally, this band-limited field propagates to the image plane, and two intensity images are captured to form the jth set of images. While the incident light is oblique, there may be pixel shift between the two intensity images due to defocus. Δd is the distance between two axially displaced
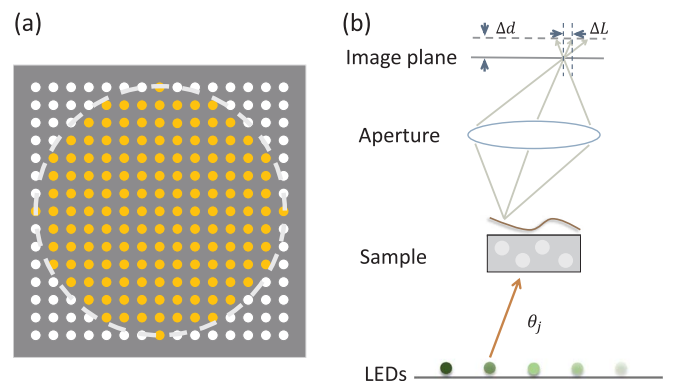

Fig. 2. (a) The LED array is used for the illumination of diffraction tomography imaging. A circular shape illumination of LEDs is adopt for the isotropic transverse resolution and higher illumination utilization of LED array. (b) Diagram of the diffraction tomography imaging setup based on a conventional microscopy in 2D. The light emitted from the jth LED scatters through the sample and exits its top surface. Then the field is propagated and limited by the finite microscope aperture at the microscope back focal plane. This band-limited field propagates to the image plane at last, and two intensity images are captured to form the jth set of images. Δd is the distance between two axially displaced planes. ΔL is the lateral shift between two intensity images under oblique incident light.
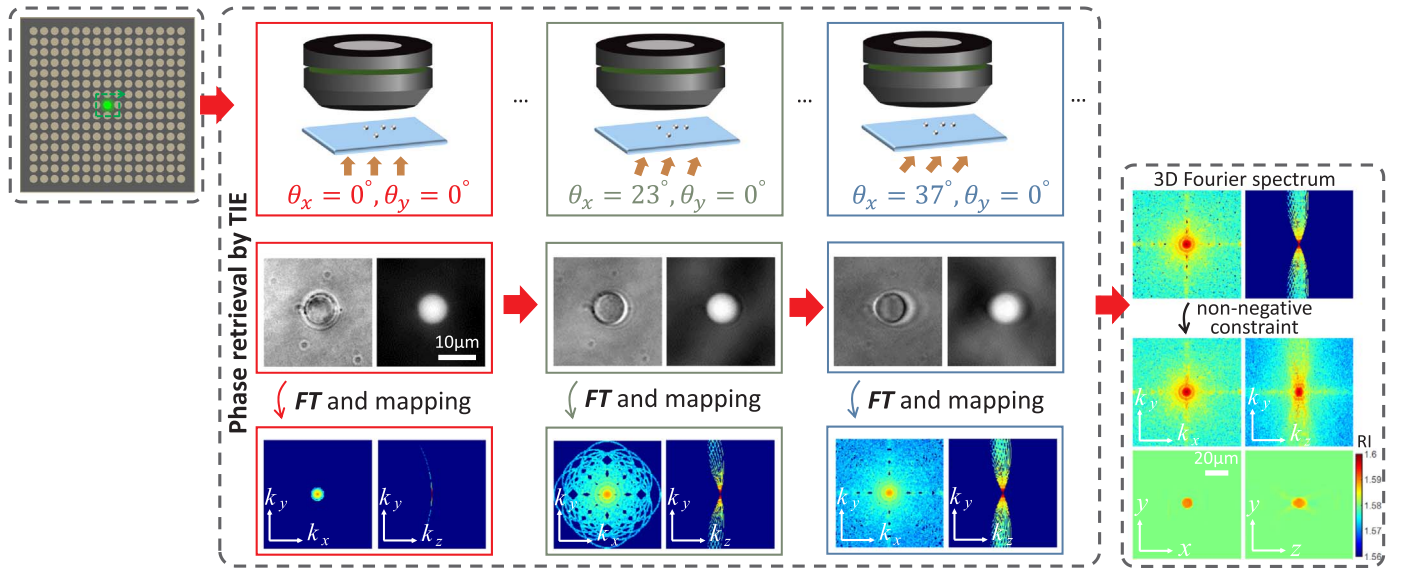
Fig. 3. The procedure of diffraction tomography imaging with TIE using a LED array. The whole process starts with the LED in the center of array, and the upright incident light is emitted from this LED. The intensity images are captured by camera and the phase is retrieved by TIE. Then the 2D Fourier transform of measured complex field is mapped to 3D Ewald sphere according to the Fourier diffraction theorem under the Rytov approximation. The next step is to turn on the next LED in array sequentially as the green dashed line and the repetition of Fourier transform and mapping. Finally, the 3D Fourier spectrum of structure is acquired and implement an iterative non-negative constraint algorithm. After constraint algorithm, some missing information is filled and the final 3D quantitative mapping of refractive index is obtained.

planes and ΔL is the lateral shift between two intensity images. For the problem of pixel shift between two intensity images, the details of image registration are introduced in the next subsection.

The whole procedure of diffraction tomography imaging with TIE using a LED array is illustrated in Fig. 3. First, the upright incident light is emitted from the LED located in the center of array. The intensity images are captured by camera and the phase is retrieved by TIE. The Fourier diffraction theorem [39] states that the 2D Fourier transform of the forward scattered complex field retrieved from one illumination angle cover a cap of sphere with same orientation in the 3D Fourier space, called Ewald sphere. Then the 2D Fourier transform of measured complex field is mapped into 3D Ewald sphere according to the Fourier diffraction theorem under the Rytov approximation. The next step is to turn on the next LED in array sequentially as shown by the dashed green line and the repetition of Fourier transform and mapping. Finally, the 3D Fourier spectrum of structure is acquired and implement an iterative non-negative constraint algorithm [32,33]. After constraint algorithm, some missing frequency components are filled and the final 3D quantitative mapping of refractive index is obtained.

3.3. Positional misalignment correction for LED array

As above mentioned, two intensity images are transversely positional misaligned at different axially planes while the illumination light is oblique. Before using the TIE to solve for phase, the sub-pixel image registration algorithms [47] are employed to match these intensity images and a ROI image must be selected. Due to the center of the LED array may not coincide with the optical axis, there are positional misalignment caused by the misplaced LED array, as shown in Fig. 1. Thus, the positional misalignment correction for LED array is necessary.

Not only the intensity images can be registered by the registration algorithms, but also the pixel shift values of image registration could be used for the correction of LED array misalignment. Under a certain illumination angle, the values of pixel shift between two intensity images are deterministic for our imaging system. The theoretical distribution shape of pixel shift values are consistent with the shape of illumination (assuming the center of the LED array coincides with the optical axis and no axial rotation). In reality, there is a system error of translation and rotation between theoretical value and actual value of

pixel shift. On a different note, the global pixel shift values of image registration for each LED can reflect the actual positional error of LED array. We could make full use of the known theoretically illumination shape and the actual pixel shift results of image registration, even though some shift values of registration algorithm are incorrect for several angles of illumination. The linear least-squares fitting of image registration result is conducted with the mathematic distribution of illumination shape:

$$\min \epsilon = \sum_{j=1}^{N} (X_j - \overline{X_j})^2 + (Y_j - \overline{Y_j})^2 \tag{4}$$

Where X_j and Y_j are the experimental results of horizontal and vertical registration pixel shift values between two intensity images corresponding to the illumination angle of jth LED, respectively. $\overline{X_j}$ and $\overline{Y_j}$ are the linear least-squares fitting results. Final linear least-squares fitting results are consistent with the distribution of illumination shape except for an error of translation and rotation. N is the total number of illumination angles, which is equal to 149. ϵ is the error between fitting and registration results in blue solid line, and the minimum value of ϵ corresponds to the optimal fitting result as shown in Fig. 4(a) in green triangle.

Fig. 4(a) shows the distribution plot of experimental pixel shift results of image registration and linear least-squares fitting results. The red dots are the results of pixel shift between two intensity images at different planes for all illumination angles. While the value of illumination angle is relatively small, the actual pixel shift is tiny. For near on axis illumination, the intensity contrast is quite low (the sample is almost transparent) especially when the object is infocus, which making it difficult to register the in-focus and defocus images accurately. In contrast, the large illumination angle provides strong phase contrast in the captured intensity images, so the registration algorithm works better. Therefore, the error between fitting and registration results in the central area is higher than marginal area. The shape of final fitting results in green triangle is the same as the theoretical illumination of LED array apart from a positional system error as Fig. 1(b) shows. Thus, the values of translation Δx, Δy and rotation angle θ caused by misplaced array could be utilized for correction of LED array. Furthermore, the comparison results of 3D tomographic reconstruction before and after positional misalignment correction for LED array are presented in subSection 4.1.
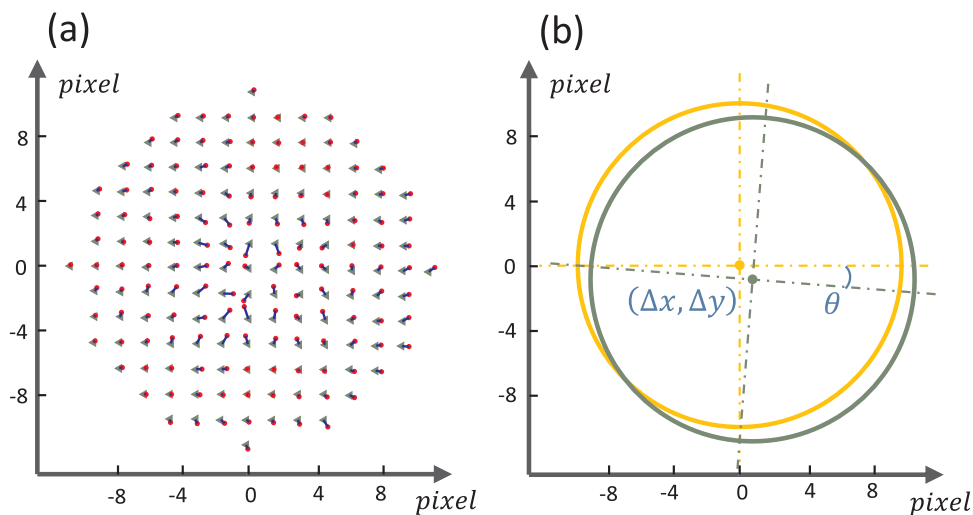
Fig. 4. (a) The distribution plot of actual pixel shift results of image registration and linear least-squares fitting results in red dot and green triangle respectively under the each illumination angle for our imaging system. The errors between two results are illustrated in blue solid line. (b) System error of positional misalignment between theoretical pixel shift distribution and linear least-squares fitting results. The values of translation Δx, Δy and rotation angle θ caused by misplaced array could be utilized for correction of LED array.

4. Results

4.1. Comparative demonstration based on micro polystyrene bead

We first demonstrate two sets of comparison results based on 10 μm micro polystyrene bead, and the bead (Polysciences, n = 1.59) is immersed in oil (Cargille, n = 1.58). The comparative quantitative phase images and profile lines of micro polystyrene bead measured by DHM and TIE under two different incident angles are shown in Fig. 5. Fig. 5(a) and (d) show the phase images of DHM measurement corresponding to upright and oblique incident light, respectively. The images of quantitative phase retrieved by TIE under two different illumination angles are illustrated in Fig. 5(b) and (e). From the cross-sectional curves of phase, we can see that the phase retrieved by TIE in green dot-dash line is more smooth and closer to the ideal value than the phase measured by DHM. But the profile line margin of DHM measurement is better than the profile line of TIE, the reason for this is that the phase retrieved by TIE is more easily influenced by the noise of intensity image globally.

Next, we present the comparison slice images of final 3D structure and Fourier spectrum in Fig. 6, which are reconstructed by 3D reconstruction approaches based on the Rytov approximation. The upper-right corner color images are the enlarged refractive index maps of centrally transverse and axial micro bead slices in blue dash line rectangle, and the two groups of results correspond to the situation of before and after positional correction for LEDs. In Fig. 6(b1) and (b2),
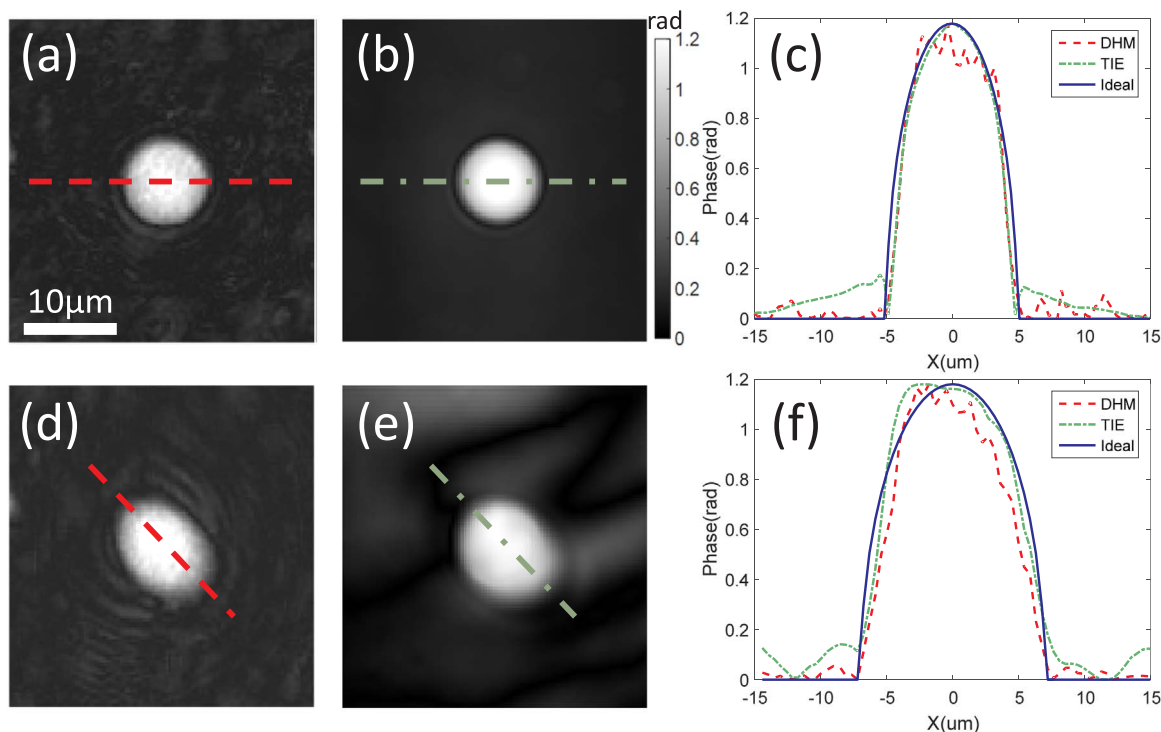

Fig. 5. The comparison results of quantitative phase measured by DHM and TIE under two different angles of illumination. (a-b) The phase images of micro polystyrene bead measured by DHM and TIE quantitatively in the case of straight incidence light. (d-e) Under the oblique illumination $\theta_x = -28°$, $\theta_y = 28°$, the quantitative phase of bead measured by DHM and TIE, respectively. (c) and (f) The comparative profile lines of quantitative phase measurement between DHM and TIE. Scale bar, 10 μm.
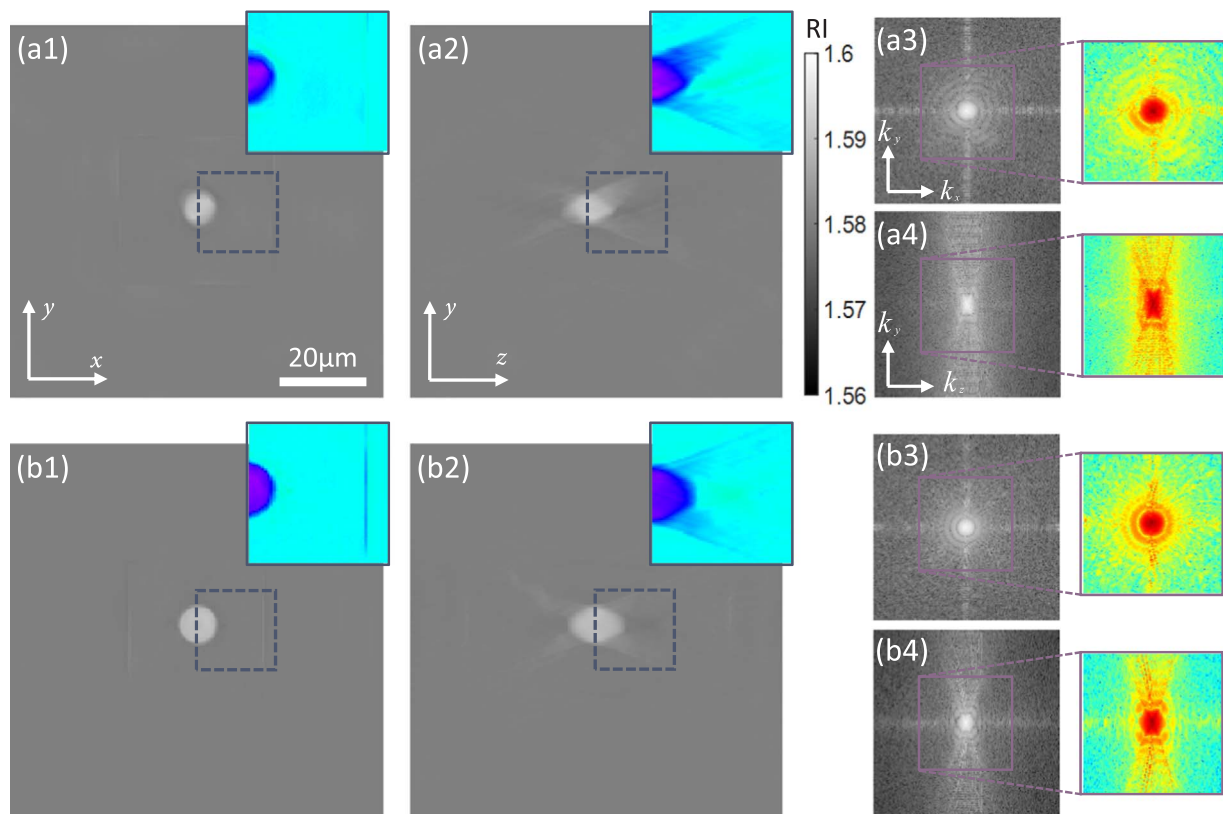
Fig. 6. The comparison images of final 3D structure and Fourier spectrum before and after positional misalignment correction for LEDs. (a) The centrally transverse and axial micro bead slice images of 3D refractive index and Fourier spectrum in the volume before positional correction. (b) The transverse and axial slice images of 3D micro bead refractive index and Fourier spectrum at the center of volume after the positional correction for LED array. Both two sets of maps are processed after 20 non-negative constraint iterations. Scale bar represents 20 μm.

the transverse slice image of final 3D structure is symmetric about the *x* axis and the axial one is basically symmetric about the *z* axis respectively. It is obvious that the reconstruction results of 3D structure in Fig. 6(b1) and (b2) are better than those in Fig. 6(a1) and (a2). The reason for this comparative results is the asymmetry of 3D Fourier spectrum. In reality, the actually angular complex fields are obtained under the illumination of misplaced LED array. But the Fourier transform of these measured fields are mapped to the cap of Ewald sphere according to the ideally geometric distribution of each LED. Some frequency components are mapped to the incorrect position in 3D spectrum domain, so this situation leads to the asymmetry of spectrum and distortion of bead structure. Nevertheless, the least-squares fitting results of the pixel shift values of image registration could accurately reflected the system error caused by the misplaced LED array, and these results can be utilized for the positional correction of misplaced LED array as well.

Finally, the measured complex fields are mapped to the correct position in Ewald sphere after positional misalignment correction for LED array. Implementing the non-negative constraint iterations algorithm, the missing-cone is filled and the accurate 3D structure could be obtained. Through the two sets of comparison results, it was proved that the TIE could be used for the phase retrieval in diffraction tomography and the misalignment correction for LED array is effective and useful for some inevitably positional errors in our system.

4.2. Experimental results

In this subsection, the performance of proposed approach is further demonstrated by tomographic imaging of polystyrene bead as well as biological samples.

By using the sets of phase and amplitude images retrieved by TIE under various angles of illumination, we map the Fourier spectrum of

complex fields into 3D Fourier space according to the Fourier diffraction theorem as shown in Fig. 3. Fig. 7 illustrates the tomographic reconstruction results of the 10 μm polystyrene bead. Fig. 7(a) and (b) show the originally central slice images of transverse and axial 3D Fourier spectrum, respectively. As a result, we may not fill the entire region of frequency space which can be seen in Fig. 7(a) and (b). The non-negative constraint iterations algorithms are used for 3D Fourier spectrum, the missing-cone is filled after 20 iterations and the reconstructed image becomes more accurate. Implementing the inverse Fourier transform to the entire 3D Fourier spectrum, the transversely and axially refractive index slice images of micro polystyrene beads at the center volume are clarified in Fig. 7(e) and (f). The relative refractive index value of polystyrene bead is 0.01 to absolute refractive index based on the oil medium refractive index (n = 1.58), and the finally absolute 3D refractive index distribution rendering of micro polystyrene beads is shown in Fig. 7(g). The comparison results of micro bead between lateral and axial line-profile are illustrated in Fig. 7(h). Due to the limited illumination angle and finite numerical aperture of the objective, the actual lateral resolution is better than the axial one. The reconstructed size of lateral line-profile is about 10 μm, while the axial value extends to 13 μm. Although the axial resolution is a bit poorer than the lateral one, the above results indicate the success of our diffraction tomography implementation based on the Rytov approximation.

Then, this diffraction tomography system is applied to an unstained paraffin section of Pandorina morum. Pandorina is a genus of green algae composed of 8, 16, or sometimes 32 cells and these cells are held together at their bases to form a sack globular colony surrounded by mucilage. The Pandorina is fixed and immersed in the embedding medium (paraffin wax, n = 1.45). Figs. 8(a)–(f) show the resulting slice images of tomograms from −10 μm to 10 μm. From these images we can clearly see the changes of refractive index and spatial location of each
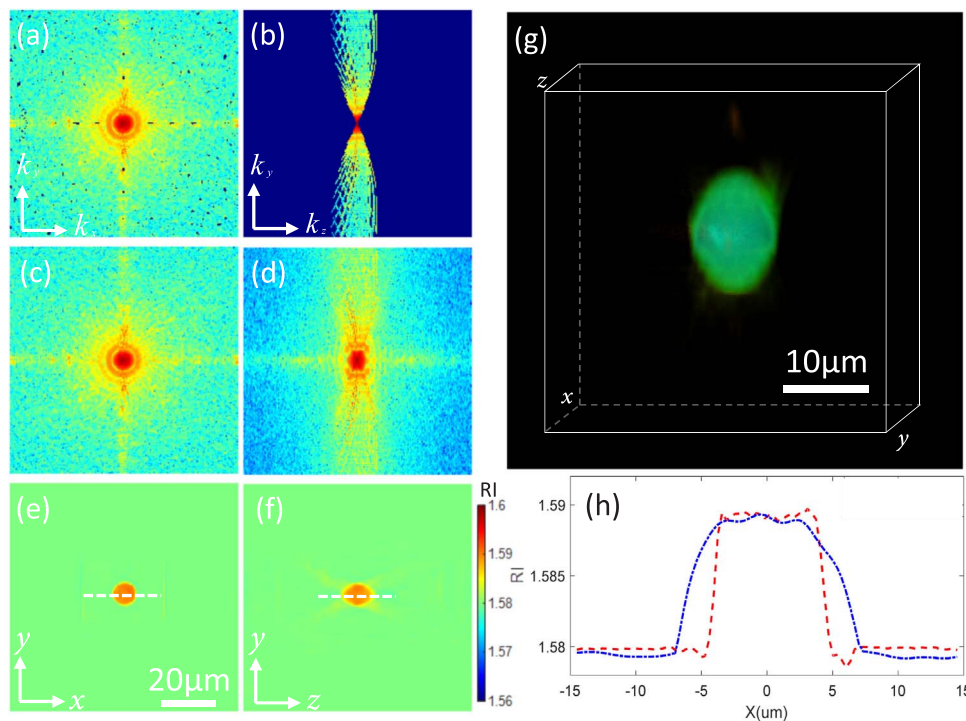
Fig. 7. Tomographic reconstruction of the 10 μm polystyrene bead. (a-b) The retrieved complex fields are mapped into 3D Fourier space according to the Fourier diffraction theorem, then the central slice images of transverse and axial 3D Fourier spectrum are acquired. (c-d) After non-negative constraint iterations algorithm, the missing-cone is filled in 3D spectrum volume. (e-f) The transverse and axial refractive index slice images of micro polystyrene beads at the center volume. (g) Final 3D refractive index distribution rendering of micro polystyrene beads. (h) The comparison results between lateral and axial line-profile. The size of lateral line-profile is about 10 μm, and the axial value extends to 13 μm. Scale bar denotes 20 and 10 μm, respectively.

cell in the Pandorina. The 3D volume image rendered by ImageJ gives more intuitive view of Pandorina in Fig. 8(g) and the color bar indicates the variation of refractive index values. It is worth noting that we extend the size of ROI intensity image to 256×256 for easier calculation and better view, the pixel value of padding area is equal to the average value of pixels on the outer edge of ROI intensity image. Thus, there will be a rectangular shape visible in the final 3D refractive index images and this rectangular shape is clearest at the in-focus position ($z = 0$ μm).

At last, the tomographic results of unstained lung cancer cell and HeLa cell are presented, and these cells are cultured in culture medium (n = 1.34). As shown in the cross-sectional slices of a reconstructed tomogram of lung cancer cell and HeLa cell along the x-y, y-z, and x-z planes in Fig. 9, the nucleolus inside individual cells have significantly

high refractive index values compared to the surrounding cytoplasm of cells. An intuitional and useful visualizations of human cancer cells refractive index distribution are demonstrated and this reconstruction methods can provide the possibility for the further study of cell morphology and pathophysiology.

5. Discussion and conclusion

In this work, we have demonstrated a novel and effective ODT imaging implementation with TIE using a LED array. A programmable LED array is employed as the illumination source and this illumination method avoids any mechanical rotation and speckle noise of the laser light source. In addition, the TIE is applied for reconstructing the quantitative phase in our system. Only two intensity images at different
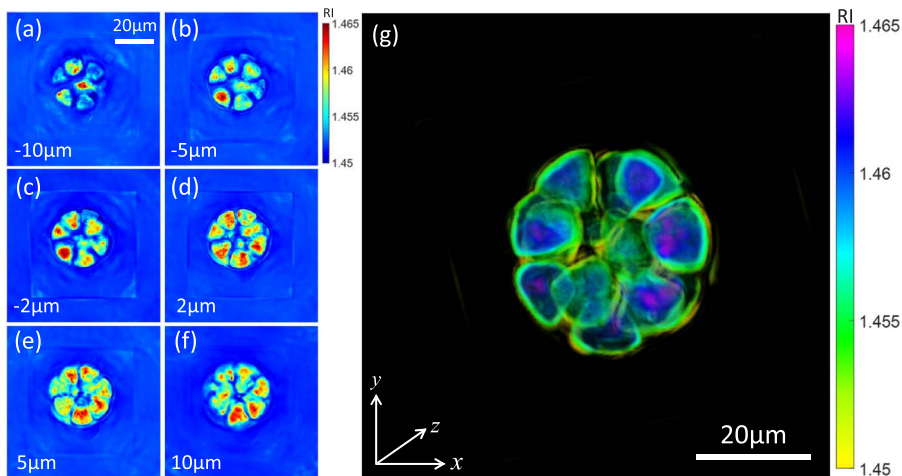

Fig. 8. The refractive index imaging results of the fixed sample of Pandorina morum. (*a-f*) The refractive index slice images of Pandorina morum at different axial planes. (g) Final 3D refractive index rendering rendered by ImageJ in volume viewer. A fast-motion movie of slice images from −10 μm to 10 μm see Media 1. Scale bar, 20 μm.
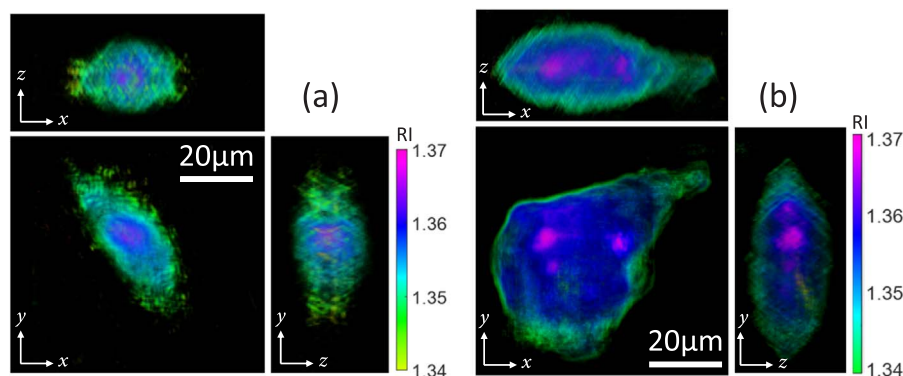
Fig. 9. 3D refractive index tomograms rendering of (a) lung cancer cell and (b) HeLa cell.

axially displaced planes are required without the need of interfero-metric device. Positional misalignment correction of LED array for more accurate measurement is added additionally. Besides, this tomography imaging setup is easily fitted into a conventional optical microscope after small modifications. The experimental results of micro polystyrene bead based on the Rytov approximation validate the success of our method. Furthermore, the 3D quantitative refractive index mapping of human cancer cells and fixed plant samples are presented as well.

Before concluding, we should note that there are still several important issues that requires further investigation or improvement. The maximum angle of the LED illumination is only about 37 degrees in this system, which is significantly restricted for the full angular range. Despite the non-negative iterative constraint algorithm can partially alleviate the generation of artifacts, the narrow angular coverage makes it impossible to obtain higher axial imaging resolution. For those high illumination angle close to the objective numerical aperture, the corresponding LED element cannot produce image with sufficient intensity, leading to a low signal-to-noise ratio (SNR). To deal with these problems, the essential way is to increase the illumination angle of LED and the additional devices may need to modify our setup, such as a smaller spacing LED array and a condenser lens.

Acknowledgments

Appendix A. Supplementary data

Supplementary data associated with this article can be found in the online version at http://dx.doi.org/10.1016/j.optlaseng.2017.03.010.

References

[1] Zernike F. Phase contrast, a new method for the microscopic observation of transparent objects. Physica 1942;9:686–98.
[2] Nomarski G, Weill A. Application à la métallographie des méthodes interférentielles à deux ondes polarisées. Rev Metall 1955;2:121–8.
[3] Schnars U, Jüptner WP. Digital recording and numerical reconstruction of holograms. Meas Sci Technol 2002;13:R85.
[4] M. K. Kim, Digital Holographic Microscopy (Springer, 2011).
[5] Popescu G, Park Y, Choi W, Dasari RR, Feld MS, Badizadegan K. Imaging red blood cell dynamics by quantitative phase microscopy. Blood Cells Mol Dis 2008;41:10–6.
[6] Bhaduri B, Pham H, Mir M, Popescu G. Diffraction phase microscopy with white light. Opt Lett 2012;37:1094–6.
[7] Bhaduri B, Tangella K, Popescu G. Fourier phase microscopy with white light. Biomed Opt Express 2013;4:1434–41.
[8] Wang Z, Millet L, Mir M, Ding H, Unarunotai S, Rogers J, et al. Spatial light

[9] interference microscopy (SLIM). Opt Express 2011;19:1016–26.
[9] Teague MR. Deterministic phase retrieval: a Green's function solution. JOSA 1983;73:1434–41.
[10] Gureyev T, Roberts A, Nugent K. Partially coherent fields, the transport-of-intensity equation, and phase uniqueness. JOSA A 1995;12:1942–6.
[11] Barty A, Nugent K, Paganin D, Roberts A. Quantitative optical phase microscopy. Opt Lett 1998;23:817–9.
[12] Waller L, Tian L, Barbastathis G. Transport of intensity phase-amplitude imaging with higher order intensity derivatives. Opt Express 2010;18:12552–61.
[13] Zuo C, Chen Q, Qu W, Asundi A. Noninterferometric single-shot quantitative phase microscopy. Opt Lett 2013;38:3538–41.
[14] Zuo C, Chen Q, Tian L, Waller L, Asundi A. Transport of intensity phase retrieval and computational imaging for partially coherent fields: the phase space perspective. Opt Lasers Eng 2015;71:20–32.
[15] Meng X, Huang H, Yan K, Tian X, Yu W, Cui H, et al. Smartphone based hand-held quantitative phase microscope using the transport of intensity equation method. Lab Chip 2017;17:104–9.
[16] Barty A, Nugent K, Roberts A, Paganin D. Quantitative phase tomography. Opt Commun 2000;175:329–36.
[17] Gorski W, Osten W. Tomographic imaging of photonic crystal fibers. Opt Lett 2007;32:1977–9.
[18] Nguyen T, Nehmetallah G, Tran D, Darudi A, Soltani P. Fully automated, high speed, tomographic phase object reconstruction using the transport of intensity equation in transmission and reflection configurations. Appl Opt 2015;54:10443–53.
[19] Nehmetallah G, Nguyen T, Fast Tomographic TIE-Based Phase Imaging Using SLM. In Digital Holography and Three-Dimensional Imaging, (Optical Society of America, 2016), DTh1E. 2.
[20] Charriere F, Marian A, Montfort F, Kuehn J, Colomb T, Cuche E, et al. Cell refractive index tomography by digital holographic microscopy. Opt Lett 2006;31:178–80.
[21] Kuś A, Dudek M, Kemper B, Kujawińska M, Vollmer A. Tomographic phase microscopy of living three-dimensional cell cultures. J Biomed Opt 2014;19:046009.
[22] Kim K, Yoon J, Shin S, Lee S, Yang S-A, Park Y. Optical diffraction tomography techniques for the study of cell pathophysiology. J Biomed Photonics Eng 2016;2.
[23] Choi W, Fang-Yen C, Badizadegan K, Oh S, Lue N, Dasari RR, et al. Tomographic phase microscopy. Nat Methods 2007;4.
[24] Sung Y, Choi W, Fang-Yen C, Badizadegan K, Dasari RR, Feld MS. Optical diffraction tomography for high resolution live cell imaging. Opt Express 2009;17:266–77.
[25] Kim M, Choi Y, Fang-Yen C, Sung Y, Dasari RR, Feld MS, et al. High-speed synthetic aperture microscopy for live cell imaging. Opt Lett 2011;36:148–50.
[26] Kostencka J, Kozacki T, Dudek M, Kujawińska M. Noise suppressed optical diffraction tomography with autofocus correction. Opt Express 2014;22:5731–45.
[27] Kuś A, Krauze W, Kujawińska M, Limited-angle holographic tomography with optically controlled projection generation, in SPIE BiOS, (International Society for Optics and Photonics, 2015), 933007-933007-933008.
[28] Shin S, Kim K, Yoon J, Park Y. Active illumination using a digital micromirror device for quantitative phase imaging. Opt Lett 2015;40:5407–10.
[29] Shin S, Kim K, Kim T, Yoon J, Hong K, Park J, Park Y, Optical diffraction tomography using a digital micromirror device for stable measurements of 4D refractive index tomography of cells, in SPIE BiOS, (International Society for Optics and Photonics, 2016), 971814-971814-971818.
[30] Isikman SO, Bishara W, Mavandadi S, Frank WY, Feng S, Lau R, Ozcan A, Lens-free optical tomographic microscope with a large imaging volume on a chip. Proceedings of the National Academy of Sciences (2011) 108, 7296–7301.
[31] Isikman SO, Bishara W, Ozcan A, Lensfree on-chip tomographic microscopy employing multi-angle illumination and pixel super-resolution, JoVE (Journal of Visualized Experiments), (2012) e4161-e4161.
[32] Tam K, Perez-Mendez V. Tomographical imaging with limited-angle input. JOSA 1981;71:582–92.
[33] Medoff BP, Brody WR, Nassi M, Macovski A. Iterative convolution backprojection algorithms for image reconstruction from limited data. JOSA 1983;73:1493–500.
[34] Kak AC, Slaney M. Principles of Computerized Tomographic Imaging. SIAM; 2001.
[35] Wolf E. Three-dimensional structure determination of semi-transparent objects from holographic data. Opt Commun 1969;1:153–6.

[36] Dändliker R, Weiss K. Reconstruction of the three-dimensional refractive index from scattered waves. Opt Commun 1970;1:323–8.

[37] Zuo C, Sun J, Zhang J, Hu Y, Chen Q. Lensless phase microscopy and diffraction tomography with multi-angle and multi-wavelength illuminations using a LED matrix. Opt Express 2015;23:14314–28.

[38] Horstmeyer R, Chung J, Ou X, Zheng G, Yang C. Diffraction tomography with Fourier ptychography. Optica 2016;3:827.

[39] Müller P, Schürmann M, Guck J, The Theory of Diffraction Tomography, arXiv:1507.00466 (2015).

[40] Zheng G, Horstmeyer R, Yang C. Wide-field, high-resolution fourier ptychographic microscopy. Nat Photon 2013;7:739–45.

[41] Tian L, Li X, Ramchandran K, Waller L. Multiplexed coded illumination for fourier ptychography with an led array microscope. Biomed Opt Express 2014;5:2376–89.

[42] Sun J, Chen Q, Zhang Y, Zuo C. Sampling criteria for Fourier ptychographic microscopy in object space and frequency space. Opt Express 2016;24:15765–81.

[43] Zuo C, Sun J, Chen Q. Adaptive step-size strategy for noise-robust Fourier ptychographic microscopy. Opt Express 2016;24:20724–44.

[44] Goodman JW. Introduction to Fourier Optics. Roberts and Company Publishers; 2005.

[45] Zuo C, Chen Q, Asundi A. Boundary-artifact-free phase retrieval with the transport of intensity equation: fast solution with use of discrete cosine transform. Opt Express 2014;22:9220–44.

[46] Zuo C, Chen Q, Li H, Qu W, Asundi A. Boundary-artifact-free phase retrieval with the transport of intensity equation ii: applications to microlens characterization. Opt Express 2014;22:18310–24.

[47] Guizar-Sicairos M, Thurman ST, Fienup JR. Efficient subpixel image registration algorithms. Opt Lett 2008;33:156–8.